Structural Effect on Electrochemical Performance of Ordered Porous Carbon Electrodes for Na-Ion Batteries

Changshin Jo,[†] Yuwon Park,[‡] Jooyoung Jeong,[†] Kyu Tae Lee,*[,‡] and Jinwoo Lee*[,†]

[†]Department of Chemical Engineering, Pohang University of Science and Technology (POSTECH), Pohang, 790-784, Korea
[‡]School of Chemical and Biological Engineering, Seoul National University, Seoul, 151-744, Korea

S *Supporting Information*

ABSTRACT: Ordered meso- or macro-porous carbons (OMCs) were applied as anodes in Na ion battery (NIB) systems. Three different block copolymers (BCPs) enabled us to control the pore sizes (6, 33, and 60 nm) while maintaining the same 2-D hexagonal structure. To exclude other effects, the factors including precursors, particle sizes, and degrees of graphitization were controlled. The structures of OMCs were characterized by nitrogen physisorption, Raman spectroscopy, X-ray analyses (XRD and SAXS), and microscopies (TEM and SEM). With a galvanostatic charge/discharge, we confirmed that OMC electrode with medium pore size (OMC-33) exhibited a higher reversible capacity of 134 mA h g^{-1} (at 20th cycle) and faster rate capability (61% retention, current densities from 50 to 5000 mA g^{-1}) than those of OMC-6, and OMC-60 electrodes. The high performance of OMC-33 is attributed to the combined effects of pore size and wall thickness which was supported by charge/discharge and electrochemical impedance spectroscopy (EIS) analyses.

KEYWORDS: *sodium ion battery, electrode, porous carbon, self-assembly, nanomaterials*
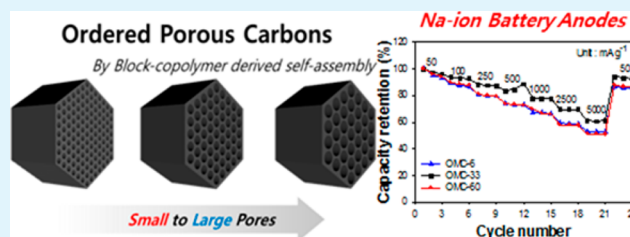
INTRODUCTION

Lithium ion battery (LIB) market continues to grow and extend their operation to the large-scale energy storage fields including electric vehicles (EVs) and renewable energy storage systems (ESSs). For this reason, numerous companies have competed with each other for securing the lithium raw material in recent years, resulting in a sharp increase in price. As a result, many researchers have investigated the electrochemical behavior of new types of charge carriers to replace expensive lithium metal. Among various candidates, sodium (Na) ion rechargeable batteries (NIBs) have been studied as alternatives to lithium ion batteries because of sodium's low price and high natural abundance.[1−3]

Recent studies have considered development of nongraphitic carbon anodes because graphite, the most-used anode material in LIBs, cannot intercalate Na ions (Na$^+$ radius: 1.06 Å, 0.3 Å larger than Li$^+$) into the graphite layer. In contrast, nongraphitic carbons can support the reversible Na$^+$ insertion/extraction reaction due to their disordered structure with void spaces. With a variety of carbon precursors, previous studies have shown reversible sodiation/desodiation reactions with capacities up to 300 mA h g^{-1} in pyrolyzed carbon hosts at different current densities and temperatures.[4−9] In addition, some nanostructured carbon electrodes have been introduced to improve the reversible capacity and rate capability. The studies have shown that not only surface area and pore volume but also their nanostructures have great influence on the electrochemical performance.[10−14]

Ordered porous materials have the merits of both nanomaterials and bulk-materials;[15] (i) highly ordered nanopores

are distributed inside micrometer-sized particles; this arrangement provides a large electrode/electrolyte interface area and an easy penetration of electrolytes into the whole particle. (ii) a pore wall a few nanometers thick, and interconnected structure result in fast solid-state diffusion of charge carriers. For example, a templated-carbon anode material containing both macro- and meso-pores has high reversible capacity of 130 mA h g^{-1} and stable cycle life.[16] However, the morphological effect of the porous structures on sodium charge/discharge behaviors has not been identified yet. Therefore, in this study, we have systematically studied the correlation how pore size and wall thickness affect the sodiation/desodiation properties of porous carbon anodes.

It is well-known that a large pore sized (>10 nm) porous carbon is hard to be synthesized by a silica-template (hard template) method and a self-assembly (soft template) using pluronic block copolymers (BCPs).[15] Therefore, it was difficult to study the systematic relationship between porous structure and electrochemical performance. However, in this work, we used lab-made BCPs to synthesize carbon particles with large pore size. We prepared different carbons with pore sizes of 6, 33, and 60 nm with the same structure (2-dimensional hexagonal) and controlled the factors that influence the electrochemical behavior, such as crystal size, surface functionality, connectivity, particle size, and micropore. We used

galvanostatic charge/discharge and electrochemical impedance spectroscopic analyses, to study the structural effects on the reversible capacity and rate capability; based on the results we propose the optimum porous structure for a high performance nongraphitic carbon anode.

■ EXPERIMENTAL SECTION

Chemicals. Tetrahydrofuran (THF), ethanol, pluronic F-127, tetraethylorthosilicate (TEOS) and hydrochloric acid (HCl, 35−38 wt %) were purchased from Sigma-Aldrich and used without purification. The resol (phenol-formaldehyde resin) was synthesized by a basic-polymerization process.[17] The poly(ethylene oxide)-*b*-poly(styrene) (PEO-*b*-PS) was prepared by atom-transfer radical-polymerization (ATRP) method.[18]

Synthesis of OMCs. The OMC-33 and OMC-60 (OMC-*x*, where *x* is the pore size) were prepared by using PEO-*b*-PS polymers (30 000 and 54 000 g mol^{-1}, PEO: 5000 g mol^{-1}).

Scheme 1. Schematic Illustration for the Block-Copolymer-Assisted Self-Assembly of Ordered Porous Carbons
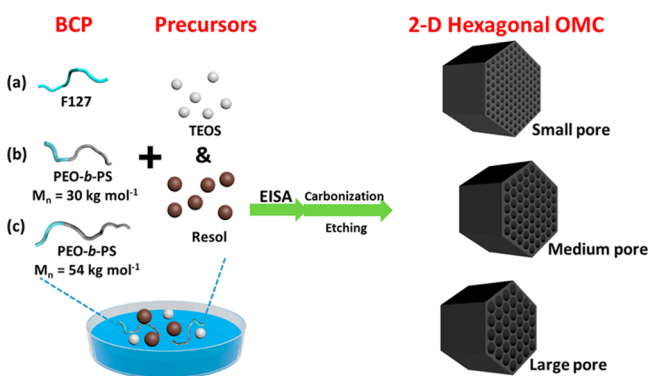
The mass ratio of hydrophobic (PS part) and hydrophilic part (PEO part, TEOS, and resol) was 1:3.5 and the mass ratio of TEOS/resol was 2.08. The PEO-*b*-PS polymers (0.2 g) were dissolved in THF. The 0.2 mL of 0.2 M HCl was added into the polymer/THF solution. After stirring for 1 h, TEOS and resol were added. After 2 h, the solution was poured into a Petri dish (40 °C) and dried for 12 h. The OMC-6 sample was prepared following the reported procedure.[17] At first, 0.8 g of pluronic F-127 was dissolved in the mixture of ethanol (4.0 g) and 0.2 M HCl (0.5 g). After 1 h, 1.04 g of TEOS and 2.5 g of 20 wt % resols' ethanolic solution were added. After 2 h, the solution was poured into a Petri dish (40 °C) and dried for 12 h. After drying at 40 °C, all samples were further dried at 100 °C in an oven for 12 h. The as-prepared films were carbonized at 1100 °C (1 °C min^{-1}) for 3 h in Ar atmosphere. Finally, the SiO$_2$ was removed by HF etching.

Characterization. The nitrogen physisorption was measured using a Tristar II 3020 instrument at 77 K (Micromeritics Instrument Co.). Small-angle X-ray scattering (SAXS) patterns were obtained using the 4C SAXS beamline at Pohang Light Source (PLS). The X-ray diffraction (XRD) patterns were measured using a Bruker D8 Advance X-ray diffractometer (Cu Kα radiation). The structure of OMCs was characterized by transmission electron microscopy (TEM, Jeol-1011) and scanning electron microscopy (SEM, S-4200 field emission SEM, Hitachi). A Raman spectrometer was employed with a laser at 514.532 nm (Ar ion laser, Horiba Jobin Yvon, LabRam Aramis) at a power of 100 μW.

Electrochemical Characterization. Slurry of 80 wt % ordered porous carbon, 10 wt % conducting agent (Super P), and 10 wt % polyvinylidene fluoride (PVdF) was casted on copper foil. The electrodes were dried at 120 °C in a vacuum oven overnight. The mass loading of active material in the
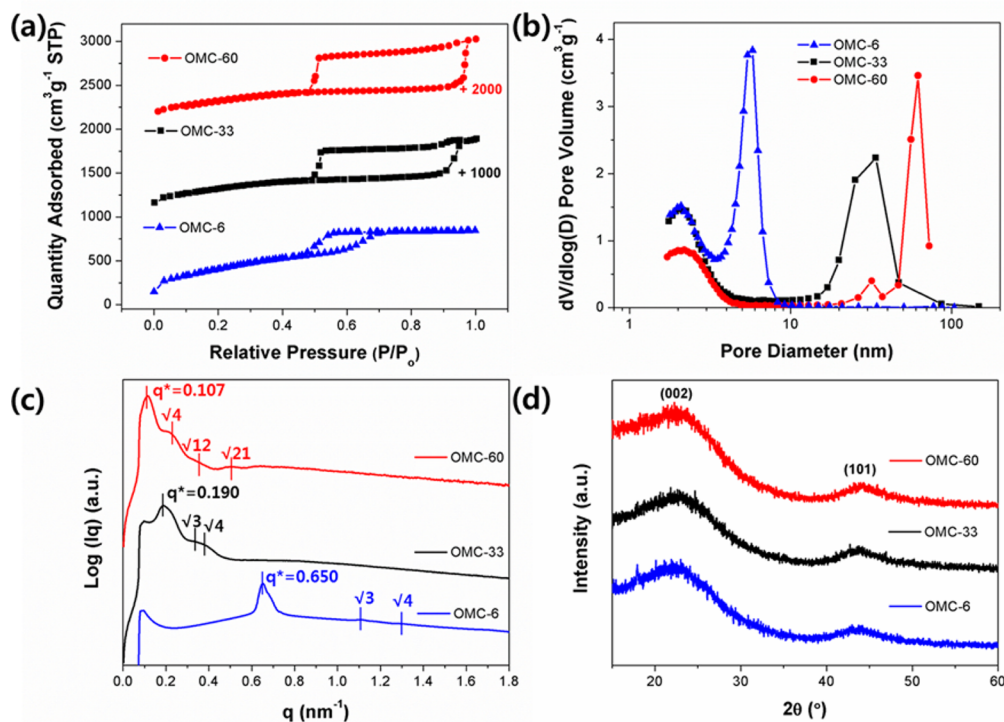

Figure 1. (a) Nitrogen physisorption isotherms (b) Barrett−Joyner−Halenda (BJH) pore size distributions (c) small-angle X-ray scattering (SAXS) patterns and (d) X-ray diffractions (XRD) patterns of each porous carbon sample.

Table 1. Physicochemical Parameters and Sodium Ion Battery Properties of OMC-x Electrodes

material	$D_{BJH}{}^a$ [nm]	$A_{BET}{}^b$ [m² g⁻¹]	$V_{Pore}{}^c$ [cm³ g⁻¹]	$T_{Wall}{}^d$ [nm]	C^e [mA h g⁻¹]	rate capability^f [%]
OMC-6	6	1472	0.99	5.2	116	52
OMC-33	33	1150	1.37	5.2	134	61
OMC-60	60	1186	1.44	7.8	94	51

^{a}Main pore size, calculated using BJH method. ^{b}BET surface area. ^{c}Total pore volume measured at P/P_o = 0.99. ^{d}Wall thickness calculated as T_{wall} = $a_0 - D_{BJH}$ ($a_0 = d_{100} \times 2/\sqrt{3}$ is unit cell parameter). ^{e}Desodation capacity delivered at the 20th cycle. ^{f}(desodation capacity at 5 A g⁻¹ rate)/(desodation capacity at 50 mA g⁻¹).

electrodes was controlled in the range of 0.7−0.95 mg cm⁻². The electrochemical characteristics were evaluated using 2032 coin cells with a Na metal anode and 1 M NaClO₄ (Aldrich, ≥ 98%) in ethylene carbonate and diethyl carbonate (1:1 v/v, PANAX ETEC Co., Ltd., Korea) electrolyte solution. Galvanostatic experiments were carried out between 0.0 and 1.7 V (vs Na/Na⁺) at current densities of 25 to 5000 mA g⁻¹ using WBCS 3000 (WonATech, Korea) at 30 °C. For electrochemical impedance spectroscopy (EIS) measurement, two-electrode cells were used under the frequency range between 500 kHz to 1 mHz under ac stimulus with 5 mV of amplitude using SP-200 (BioLogic).

■ RESULTS AND DISCUSSION

We designed three porous carbons by applying BCP-assisted self-assembly using pluronic F-127 and poly(ethylene oxide)-b-poly(styrene) (PEO-b-PS) as structure-directing agents (Scheme 1).[17,19−23] The F-127 polymer was chosen for directing carbon to form small pores, and PEO-b-PSs with two different M_n values (30 000 and 54 000 g mol⁻¹, respectively) were used to develop carbon with medium and large-pores. By adjusting the BCP/precursors ratio, we induced the interaction between resol (nongraphitic carbon source) and tetraethylorthosilicate (TEOS, silica source) with BCPs, resulting in construction of 2-D hexagonal pore arrays. All BCP/precursor composites were carbonized at 1100 °C under Ar atmosphere, followed by silica etching process. To exclude the particle size effect, the carbon samples were ground to ~5 μm without collapse of porous structure (Supporting Information Figure S1).

The structures of the three porous carbon samples were characterized using nitrogen physisorption and X-ray analyses (Figure 1). All samples showed typical type-IV N₂ adsorption−desorption isotherms with shape capillary condensations at 0.67, 0.95, and 0.97 P/P₀ for carbons with small, medium, and large pores, respectively (Figure 1a); these results indicate that the pores are uniformly distributed in each sample. The Barrett−Joyner−Halenda (BJH) pore size distributions (Figure 1b) were calculated from the adsorption branches of the isotherms. All samples had micropores (<2 nm) caused by the pyrolysis of carbon precursor and the SiO₂ etching process. The calculated main pore sizes were 6, 33, and 60 nm, respectively. Here, the carbon samples are denoted as ordered meso- or macro-porous carbon (OMC-x, where x is the main pore size). The Brunauer−Emmett−Teller (BET) surface areas of OMCs were 1472 (OMC-6), 1150 (OMC-33) and 1186 m² g⁻¹ (OMC-60). Although the surface area did not change with pore size, OMCs had high surface area (>1000 m² g⁻¹) due to the existence of micropores. The pore volumes of OMCs were 0.99 (OMC-6), 1.37 (OMC-33), and 1.44 cm³ g⁻¹ (OMC-60). The large pores and high pore volume are favorable for electrolyte penetration, which allows effective ion conduction to the internal surfaces of the OMCs.[24,25]
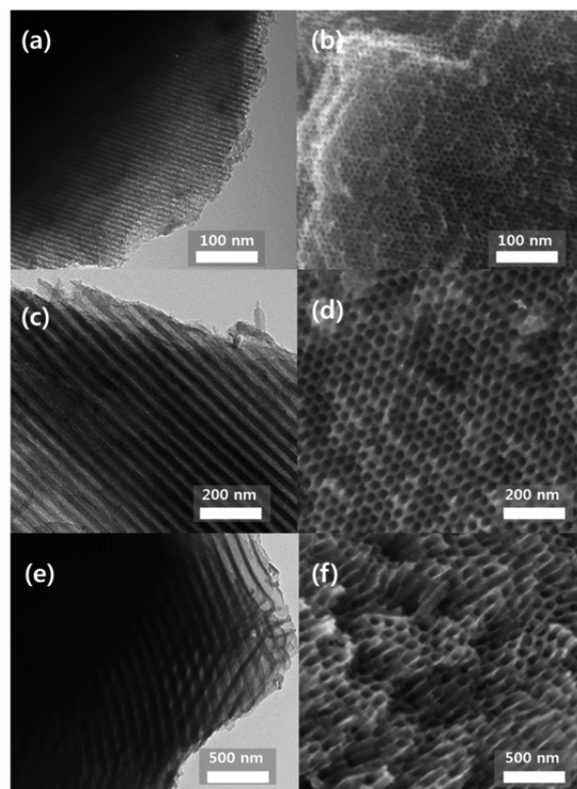

Figure 2. Transmission electron microscopy (TEM) and scanning electron microscopy (SEM) images for (a, b) OMC-6, (c, d) OMC-33, and (e, f) OMC-60 samples.

Small angle X-ray scattering (SAXS) patterns (Figure 1c) of all OMC samples showed several peaks at positions (q^m/q^*) of $1:3^{1/2}:4^{1/2}:12^{1/2}:21^{1/2}$, where q^m and q^* are the scattering positions and the first peak position, respectively. The peak positions indicate that the OMCs have a cylindrical 2-D hexagonal mesoporous structure with long-range order.[26] The $d_{spacing}$ values ($d_{100} = 2\pi/q^*$) of OMCs were 9.7 (OMC-6), 33.1 (OMC-33), and 58.7 nm (OMC-60). The wall thickness of OMCs can be estimated from the unit-cell parameter (a_o) and BJH pore size (Table 1). The wall thicknesses were 5.2 nm (OMC-6), 5.2 nm (OMC-33), and 7.8 nm (OMC-60), respectively. The wall thickness of OMC-6 is equal to that of OMC-33. This result indicates that all factors, except pore sizes, are well controlled to be similar for the two samples. Therefore, it is possible to confirm the pore size effects of OMCs by comparing the electrochemical performance of OMC-6 and OMC-33 electrodes. It is expected that the large pores facilitate the electrolyte penetration (electrolyte wetting) and ionic motion inside the OMC particles. On the other hand, the wall thickness effects also can be deduced by comparing OMC-60 electrode with other two electrodes. Difference in wall
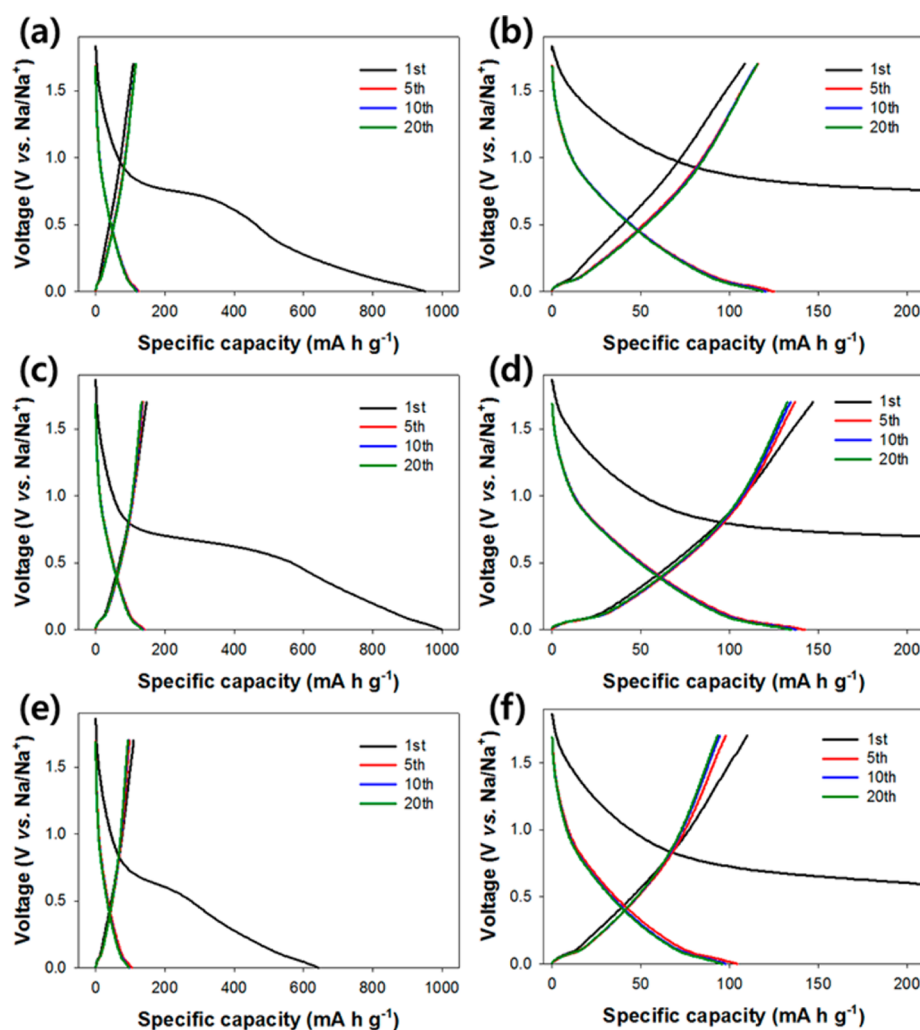
Figure 3. Voltage profiles of (a, b) OMC-6, (c, d) OMC-33, and (e, f) OMC-60 electrodes obtained at current density 25 mA g^{-1} (0−1.7 V vs Na/Na$^+$).

thickness can influence the solid-state diffusion process; for example, a hollow spherical carbon electrode exhibited a much higher sodium charge capacity and better rate capability than did a spherical carbon electrode because of the short solid-state diffusion length in the hollow structure.[11] Therefore, in our case, the solid-state diffusion process is expected to be more active in the carbon with the thin walls (OMC-6 and OMC-33, 5.2 nm) than in the carbon with thick walls.

The X-ray diffraction (XRD) patterns of OMCs showed two broad peaks at 22.5° and 44.0−44.2°, which correspond to the (002) and (101) diffractions, respectively. The interlayer distance (d_{200}) in OMCs was 0.395 nm, which is larger than that of graphitic carbon (0.335 nm). The broad interlayer distance is a typical characteristic of nongraphitic carbon which provides easier intercalation of Na$^+$ compared with that of graphitic carbon. Raman spectroscopy analysis was conducted to evaluate the degree of graphitization (Supporting Information Figure S2). All carbon materials showed peaks at ~1590 and ~1340 cm^{-1} that can be assigned to the G and D bands, respectively. The peak positions and the similar I_D/I_G values of OMCs (0.92− 0.95) imply that the OMCs, which were carbonized under the same condition, have similar degrees of graphitization.

Transmission electron microscopy (TEM) and scanning electron microscopy (SEM) images of the different OMCs

were taken (Figure 2). The TEM images viewed from the [100] direction reveal highly ordered 2-D hexagonal structure, formed by BCP-assisted self-assembly. The wall thickness/pore size ratio in TEM images appears different from the results of BET and SAXS analyses, but this apparent difference can be ascribed to distortion by the transmission light angle and the arrangement of sample. However, SEM images viewed from [001] direction provide clear information on the structure of OMCs. The observed pore size and wall thickness values were consistent with the pore size distribution from N$_2$ physisorption measurement and the wall thickness calculation. The structural characterization revealed that all OMCs have highly ordered and identically formed 2-D hexagonal porous structures with the same conditions except pore size and wall thickness.

To investigate the role of pore size and wall thickness on the electrochemical performance of disordered carbon electrodes, the cycle and rate performance of OMCs with various pore sizes and wall thicknesses were compared using a galvanostatic charge/discharge test. Voltage profiles of OMC electrodes were obtained at a constant current density of 25 mA g^{-1} in the voltage range of 0−1.7 V (Figure 3). All OMC electrodes showed similar sodiation behavior during the first cycle: (i) a short sloped region from OCV to 0.8 V, (ii) a plateau at about 0.8 V, and (iii) a sloped region to 0 V (see their differential
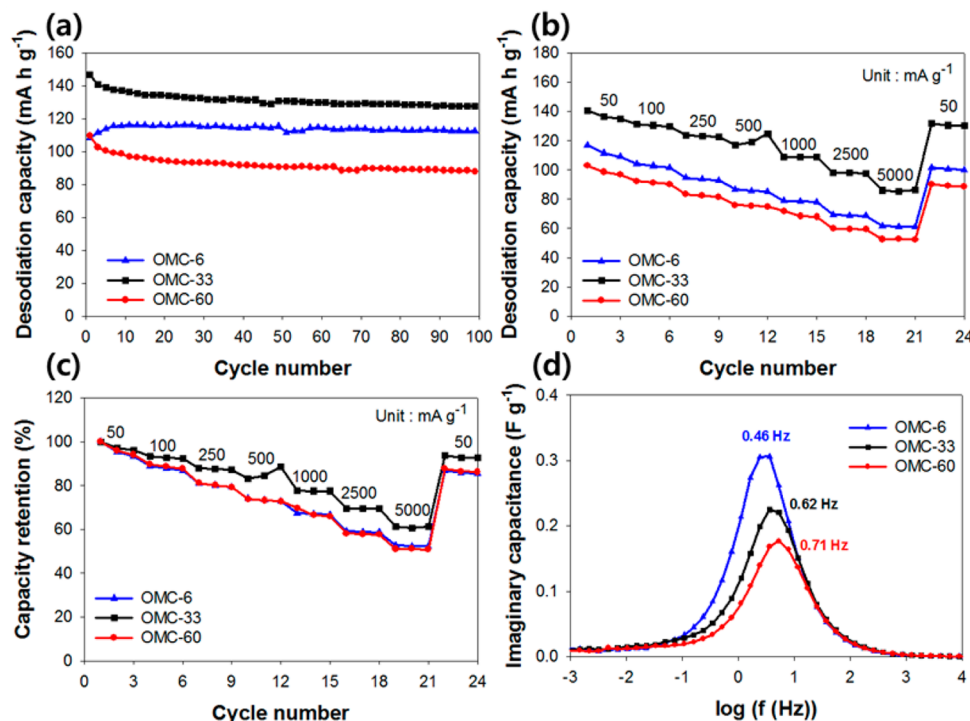
Figure 4. (a) Cycle performance, (b) rate performance, and (c) the normalized rate performance of OMC electrodes. (d) Imaginary capacitance plots of OMC electrodes obtained from EIS analysis.

capacity plots in Supporting Information Figure S3). Unlike sodiation during the first cycle, only sloping curves were observed during desodiation and subsequent cycles; this observation indicates that the plateau at ~0.8 V during the first cycle is irreversible capacity loss due to irreversible electrolyte decomposition. The larger irreversible capacities were obtained in OMC-6 and OMC-33 electrodes (>800 mA h g^{-1}) compared with that of OMC-60 electrode (>500 mA h g^{-1}). In previous study, it was reported that the irreversible capacity in graphite electrode is generally proportional to the BET surface area of the samples. However, in nongraphitic carbon case, there are complicated contributions in irreversible capacity from various factors, such as formation of solid electrolyte interphase (SEI), reaction with functional groups or absorbed molecules after exposure to air, and ion insertion into the cavities in carbons.[27] This capacity loss can be reduced by controlling pyrolysis conditions, surface modification, or electrolyte optimization.[27,28] Beginning in the second cycle, all electrodes exhibited stable voltage profiles with reversible capacities (at the 20th cycle) of 116 (OMC-6), 134 (OMC-33), and 94 mA h g^{-1} (OMC-60). The OMC-33 electrode delivered the highest reversible capacity, followed by the OMC-6 and OMC-60 electrodes. Because other variables such as precursors and particle sizes were controlled, the different electrochemical performance of OMC electrodes is attributed to their different pore sizes and wall thicknesses.

The cycle performance of OMC electrodes were obtained at current density of 25 mA g^{-1} (Figure 4a). All electrodes showed stable cycle performance regardless of pore size and wall thickness, and their reversible capacities of OMC electrodes at the 100th cycle were 113 (OMC-6), 128 (OMC-33), and 88 mA h g^{-1} (OMC-60). The reversible capacities are comparable to the capacity values reported in previous studies.[4−6,16] Moreover, the ordered porous structure was

observed even after 100 cycles, indicating that the porous carbon structure of the sample is well preserved during repetitive sodiation/desodiation processes and the electrolyte decomposition is not severe on the surface of carbon (ex-situ TEM images in Supporting Information Figure S4). However, the rate capability was obviously affected by the pore size and wall thickness. The reversible capacities of OMC electrodes were measured at various current densities from 50 to 5000 mA g^{-1} (Figure 4b), and their capacity values were normalized (Figure 4c). Charge−discharge profiles under different current densities are shown in Supporting Information Figure S5. As current density increases, reversible capacity decreases in all electrodes. However, three-carbon electrodes show similar charge−discharge profiles under high C-rate conditions, thereby indicating that all electrodes store Na$^+$ with similar charging processes under different current densities. At the current density of 5 A g^{-1}, the OMC-33 electrode delivered 61% of the reversible capacity at 50 mA g^{-1}, which is higher than the 52 and 51% delivered by the OMC-6 and OMC-60 electrodes, respectively. Compared to OMC-6 electrode, OMC-33 electrode exhibited faster rate capability and higher specific capacity, mainly due to the large pores. On the other hand, in OMC-33 vs OMC-60 case, although pore size increased from 33 to 60 nm, the electrochemical performance of OMC-60 was poorer than OMC-33. With the results, we can deduce that the improvement of OMC electrode performance is proportional to the main pore size and inversely proportional to the wall thickness. Particularly, it can be also deduced that the wall thickness tends to contribute more to electrochemical performance.

To clarify the pore size effect on the rate capability of OMC electrodes, electrochemical impedance spectroscopy (EIS) analysis was performed (Figure 4d and Supporting Information Figure S6) under a symmetric cell (SC) configuration

consisting of two identical OMC electrodes; the state of charge (SOC) for OMC electrodes was maintained at 50% by the consequent electrochemical sodiation, desodiation, and further half-sodiation. The imaginary capacitance plot (Figure 4d) was calculated from the complex impedance data in the region of high frequency.[29] The peak position is closely related to the resistance regarding the ionic conduction inside the internal pores of mesoporous carbons.[30] Increase in the frequency of peak position indicates decrease in resistance to ionic conduction in pores. The frequency at which the peak occurred increase as the pore size increased; this means that the fast ionic conduction is favorable in large pores. For example, Na^+ actively intercalated into amorphous TiO_2 tubes with large diameter, but not into narrower tubes (<45 nm).[24]

However, the OMC-33 electrode exhibited the best rate performance, whereas the OMC-60 electrode had the largest pore size. This result can be ascribed to the aforementioned wall thickness effect. The OMC-33 has the thinner walls than the OMC-60, so the OMC-33 has a smaller solid-state diffusion length and therefore smaller mass-transfer resistance than OMC-60. As pore size increase, in OMC-33 vs OMC-60 case, the increase in the speed of ionic conduction in pores was offset by the decrease in solid-state diffusion. Therefore, the combined effects of pore size and wall thickness resulted in the better capacity and rate capability of OMC-33 than OMC-60, despite the pore size being larger in OMC-60 than in OMC-33. Although simultaneous control of pore size and wall thickness in ordered porous carbons is a difficult task, this result is meaningful in that the electrochemical performance of porous carbon can be improved by controlling pore size and wall thickness.

CONCLUSION

In summary, we studied the pore size and wall thickness effects on the sodiation and desodiation of 2-D hexagonal porous carbon electrodes. The electrode performance of porous structured nongraphitic carbon can be improved by increasing pore size and decreasing wall thickness. This result implies that the pore size and wall thickness must be considered when fabricating porous NIB electrode materials. The knowledge obtained in this work will be useful to guide design of ordered porous materials for Na ion batteries.

ASSOCIATED CONTENT

ⓢ Supporting Information

SEM, nitrogen physisorption after grinding process, Raman spectra for OMCs and differential capacity, TEM images after cycling, Nyquist plots for carbon electrodes. The Supporting Information is available free of charge on the ACS Publications website at DOI: 10.1021/acsami.5b03186.

AUTHOR INFORMATION

Corresponding Authors
*(K.T.L.) E-mail: ktlee@snu.ac.kr.
*(J.L.) E-mail: jinwoo03@postech.ac.kr.
Notes
The authors declare no competing financial interest.

ACKNOWLEDGMENTS

REFERENCES

(1) Slater, M. D.; Kim, D.; Lee, E.; Johnson, C. S. Sodium-Ion Batteries. *Adv. Funct. Mater.* **2013**, *23*, 947−958.
(2) Ellis, B. L.; Nazar, L. F. Sodium and Sodium-ion Energy Storage Batteries. *Curr. Opin. Solid State Mater. Sci.* **2012**, *16*, 168−177.
(3) Hong, S. Y.; Kim, Y.; Park, Y.; Choi, A.; Choi, N.-S.; Lee, K. T. Charge Carriers in Rechargeable Batteries: Na ions vs. Li ions. *Energy Environ. Sci.* **2013**, *6*, 2067−2081.
(4) Doeff, M. M.; Ma, Y.; Visco, S. J.; De Jonghe, L. C. Electrochemical Insertion of Sodium into Carbon. *J. Electrochem. Soc.* **1993**, *140*, L169−L170.
(5) Stevens, D. A.; Dahn, J. R. The Mechanisms of Lithium and Sodium Insertion in Carbon Materials. *J. Electrochem. Soc.* **2001**, *148*, A803−A811.
(6) Alcántara, R.; Jiménez-Mateos, J. M.; Lavela, P.; Tirado, J. L. Carbon black: a Promising Electrode Material for Sodium-ion Batteries. *Electrochem. Commun.* **2001**, *3*, 639−642.
(7) Stevens, D. A.; Dahn, J. R. High Capacity Anode Materials for Rechargeable Sodium-Ion Batteries. *J. Electrochem. Soc.* **2000**, *147*, 1271−1273.
(8) Thomas, P.; Billaud, D. Electrochemical Insertion of Sodium into Hard Carbons. *Electrochim. Acta* **2002**, *47*, 3303−3307.
(9) Alcántara, R.; Lavela, P.; Ortiz, G. F.; Tirado, J. L. Carbon Microspheres Obtained from Resorcinol-Formaldehyde as High-Capacity Electrodes for Sodium-Ion Batteries. *Electrochem. Solid-State Lett.* **2005**, *8*, A222−A225.
(10) Cao, Y.; Xiao, L.; Sushko, M. L.; Wang, W.; Schwenzer, B.; Xiao, J.; Nie, Z.; Saraf, L. V.; Yang, Z.; Liu, J. Sodium Ion Insertion in Hollow Carbon Nanowires for Battery Applications. *Nano Lett.* **2012**, *12*, 3783−3787.
(11) Tang, K.; Fu, L.; White, R. J.; Yu, L.; Titirici, M.-M.; Antonietti, M.; Maier, J. Hollow Carbon Nanospheres with Superior Rate Capability for Sodium-Based Batteries. *Adv. Energy Mater.* **2012**, *2*, 873−877.
(12) Komaba, S.; Murata, W.; Ishikawa, T.; Yabuuchi, N.; Ozeki, T.; Nakayama, T.; Ogata, A.; Gotoh, K.; Fujiwara, K. Electrochemical Na Insertion and Solid Electrolyte Interphase for Hard-Carbon Electrodes and Application to Na-Ion Batteries. *Adv. Funct. Mater.* **2011**, *21*, 3859−3867.
(13) Luo, W.; Schardt, J.; Bommier, C.; Wang, B.; Razink, J.; Simonsen, J.; Ji, X. Carbon Nanofibers Derived from Cellulose Nanofibers as a Long-life Anode Material for Rechargeable Sodium-ion Batteries. *J. Mater. Chem. A* **2013**, *1*, 10662−10666.
(14) Ding, J.; Wang, H.; Li, Z.; Kohandehghan, A.; Cui, K.; Xu, Z.; Zahiri, B.; Tan, X.; Lotfabad, E. M.; Olsen, B. C.; Mitlin, D. Carbon Nanosheet Frameworks Derived from Peat Moss as High Performance Sodium Ion Battery Anodes. *ACS Nano* **2013**, *7*, 11004−11015.
(15) Ye, Y.; Jo, C.; Jeong, I.; Lee, J. Functional Mesoporous Materials for Energy Applications: Solar cells, Fuel cells, and Batteries. *Nanoscale* **2013**, *5*, 4584−4605.
(16) Wenzel, S.; Hara, T.; Janek, J.; Adelhelm, P. Room-temperature Sodium-ion Batteries: Improving the Rate Capability of Carbon Anode Materials by Templating Strategies. *Energy Environ. Sci.* **2011**, *4*, 3342−3345.
(17) Liu, R.; Shi, Y.; Wan, Y.; Meng, Y.; Zhang, F.; Gu, D.; Chen, Z.; Tu, B.; Zhao, D. Triconstituent Co-assembly to Ordered Mesostructured Polymer−Silica and Carbon−Silica Nanocomposites and Large-Pore Mesoporous Carbons with High Surface Areas. *J. Am. Chem. Soc.* **2006**, *128*, 11652−11662.
(18) Hwang, J.; Jo, C.; Hur, K.; Lim, J.; Kim, S.; Lee, J. Direct Access to Hierarchically Porous Inorganic Oxide Materials with Three-Dimensionally Interconnected Networks. *J. Am. Chem. Soc.* **2014**, *136*, 16066−16072.

(19) Lim, E.; Kim, H.; Jo, C.; Chun, J.; Ku, K.; Kim, S.; Lee, H. I.; Nam, I.-S.; Yoon, S.; Kang, K.; Lee, J. Advanced Hybrid Supercapacitor Based on a Mesoporous Niobium Pentaoxide/Carbon as High-Performance Anode. *ACS Nano* **2014**, *8*, 8968−8978.

(20) Hwang, J.; Woo, S. H.; Shim, J.; Jo, C.; Lee, K. T.; Lee, J. One-Pot Synthesis of Tin-Embedded Carbon/Silica Nanocomposites for Anode Materials in Lithium-Ion Batteries. *ACS Nano* **2013**, *7*, 1036−1044.

(21) Jo, C.; Hwang, J.; Song, H.; Dao, A. H.; Kim, Y.-T.; Lee, S. H.; Hong, S. W.; Yoon, S.; Lee, J. Block-Copolymer-Assisted One-Pot Synthesis of Ordered Mesoporous WO_{3-x}/Carbon Nanocomposites as High-Rate-Performance Electrodes for Pseudocapacitors. *Adv. Funct. Mater.* **2013**, *23*, 3747−3754.

(22) Jo, C.; Kim, Y.; Hwang, J.; Shim, J.; Chun, J.; Lee, J. Block Copolymer Directed Ordered Mesostructured $TiNb_2O_7$ Multimetallic Oxide Constructed of Nanocrystals as High Power Li-Ion Battery Anodes. *Chem. Mater.* **2014**, *26*, 3508−3514.

(23) Li, Y.; Wei, J.; Luo, W.; Wang, C.; Li, W.; Feng, S.; Yue, Q.; Wang, M.; Elzatahry, A. A.; Deng, Y.; Zhao, D. Tricomponent Coassembly Approach To Synthesize Ordered Mesoporous Carbon/Silica Nanocomposites and Their Derivative Mesoporous Silicas with Dual Porosities. *Chem. Mater.* **2014**, *26*, 2438−2444.

(24) Xiong, H.; Slater, M. D.; Balasubramanian, M.; Johnson, C. S.; Rajh, T. Amorphous TiO_2 Nanotube Anode for Rechargeable Sodium Ion Batteries. *J. Phys. Chem. Lett.* **2011**, *2*, 2560−2565.

(25) Lee, K. T.; Lytle, J. C.; Ergang, N. S.; Oh, S. M.; Stein, A. Synthesis and Rate Performance of Monolithic Macroporous Carbon Electrodes for Lithium-Ion Secondary Batteries. *Adv. Funct. Mater.* **2005**, *15*, 547−556.

(26) Lee, J.; Christopher Orilall, M.; Warren, S. C.; Kamperman, M.; DiSalvo, F. J.; Wiesner, U. Direct Access to Thermally Stable and Highly Crystalline Mesoporous Transition-Metal Oxides with Uniform Pores. *Nat. Mater.* **2008**, *7*, 222−228.

(27) Buiel, E.; Dahn, J. R. Li-insertion in Hard Carbon Anode Materials for Li-ion Batteries. *Electcrochim. Acta* **1999**, *45*, 121−130.

(28) Zhang, S. S. A Review on Electrolyte Additives for Lithium-ion Batteries. *J. Power Sources* **2006**, *162*, 1379−1394.

(29) Chmiola, J.; Yushin, G.; Dash, R.; Gogotsi, Y. Effect of Pore Size and Surface Area of Carbide Derived Carbons on Specific Capacitance. *J. Power Sources* **2006**, *158*, 765−772.

(30) Yoon, S.; Jang, J. H.; Ka, B. H.; Oh, S. M. Complex Capacitance Analysis on Rate Capability of Electric-double Layer Capacitor (EDLC) Electrodes of Different Thickness. *Electrochim. Acta* **2005**, *50*, 2255−2262.